Research paper

A cross scale investigation of galena oxidation and controls on mobilization of lead in mine waste rock

Zhongwen Bao [a,*], Tom Al [b], Martin Couillard [c], Glenn Poirier [d], Jeff Bain [a], Heather K. Shrimpton [a], Y. Zou Finfrock [e,f], Antonio Lanzirotti [g], Dogan Paktunc [h], Emily Saurette [a], Yongfeng Hu [e], Carol J. Ptacek [a], David W. Blowes [a]

[a] University of Waterloo, Department of Earth and Environmental Sciences, 200 University Avenue West, N2L 3G1 Waterloo, ON, Canada
[b] University of Ottawa, Department of Earth and Environmental Sciences, 75 Laurier Ave. East, K1N 6N5 Ottawa, ON, Canada
[c] Energy, Mining and Environment Portfolio, National Research Council Canada, 1200 Montreal Road, K1A 0R6 Ottawa, Ontario, Canada
[d] Canadian Museum of Nature, Ottawa, Ontario K1P 6P4, Canada
[e] Science Division, Canadian Light Source Inc., 44 Innovation Boulevard, S7N 2V3 Saskatoon, SK, Canada
[f] Advanced Photon Source, Argonne National Laboratory, CLS@APS Sector 20, 9700 S. Cass Avenue, 60439 Argonne, IL, United States
[g] Center for Advanced Radiation Sources, University of Chicago, Chicago, IL 60637, United States
[h] Canmet MINING, Natural Resources Canada, 555 Booth Street, K1A 0G1 Ottawa, ON, Canada

ARTICLE INFO

ABSTRACT

Galena and Pb-bearing secondary phases are the main sources of Pb in the terrestrial environment. Oxidative dissolution of galena releases aqueous Pb and SO_4 to the surficial environment and commonly causes the formation of anglesite (in acidic environments) or cerussite (in alkaline environments). However, conditions prevalent in weathering environments are diverse and different reaction mechanisms reflect this variability at various scales. Here we applied complementary techniques across a range of scales, from nanometers to 10 s of meters, to study the oxidation of galena and accumulation of secondary phases that influence the release and mobilization of Pb within a sulfide-bearing waste-rock pile. Within the neutral-pH pore-water environment, the oxidation of galena releases Pb ions resulting in the formation of secondary Pb-bearing carbonate precipitates. Cerussite is the dominant phase and shannonite is a possible minor phase. Dissolved Cu from the pore water reacts at the surface of galena, forming covellite at the interface. Nanometer scale characterization suggests that secondary covellite is intergrown with secondary Pb-bearing carbonates at the interface. A small amount of the S derived from galena is sequestered with the secondary covellite, but the majority of the S is oxidized to sulfate and released to the pore water.

1. Introduction

Mining activities including ore excavation and metal extraction generate large amounts of mine wastes (sulfide-bearing waste rock and mill tailings). Weathering and leaching of these wastes can cause continuous inputs of acidity and toxic metal(loid)s (e.g. As, Cd, Co, Cu, Hg, Ni, Pb, Zn, Sb, and Se) to surrounding groundwater and surface water. A variety of physical, chemical and biological processes (e.g. advection and diffusion of reactants such as O_2 and H_2O, and microbially catalyzed reactions) contribute to the oxidative dissolution of sulfide minerals. The pH-driven dissolution of minerals, precipitation of secondary mineral phases, sorption/desorption at mineral surfaces can moderate the concentrations of dissolved contaminants that degrade the quality of meteoric water and groundwater that flows through these wastes, which may have a deleterious effect on the surrounding environment (Hudson-Edwards et al., 2011; Jamieson, 2011; Nordstrom, 2011; Blowes et al., 2014; Amos et al., 2015).

Lead is among the most toxic environmental contaminants (Badawy et al., 2002; Cheng and Hu, 2010). Its widespread industrial use and the weathering of natural mineral deposits have resulted in anthropogenic and natural dispersion of Pb throughout the terrestrial environment (Cheng and Hu, 2010; Renberg et al., 1994; Brown Jr. et al., 1999). Mining of galena [PbS] ores accounts for approximately half of lead materials used today, with another half is derived from lead recycling

([Blowes et al., 2014](#)). Weathering of galena-rich ore deposits and mine wastes can release Pb to the surrounding groundwater and surface water, and cause the formation of a wide range of secondary Pb-bearing minerals such as anglesite [$PbSO_4$], cerussite [$PbCO_3$], pyromorphite [$Pb_5(PO_4)_3Cl$], hydrocerussite [$Pb_3(CO_3)_2(OH)_2$], plumbojarosite [$PbFe_6(SO_4)_4(OH)_{12}$], and plumbonacrite [$Pb_5O(OH)_2(CO_3)_3$]. These Pb-bearing secondary minerals display a wide range of solubility, as indicated by their respective solubility-product constants (K_{sp}; *SI Appendix*, [Table S1](#)), which influences the release, mobility and bioavailability of dissolved Pb, and the eventual impact to human health and the environment ([Badawy et al., 2002; Brown Jr. et al., 1999](#)).

Decision making for remediation at operating and abandoned mine sites can benefit from the integration of site-specific characterization of hydrological, geochemical, mineralogical, and microbial conditions and hydrogeochemical modeling ([Nordstrom and Alpers, 1999; Nordstrom et al., 2000](#)). Each of these areas of interest require comprehensive investigative effort; the present study focuses on mineralogical characterization, a key focus in mine-waste management ([Jamieson, 2011](#)). Previous environmental mineralogy research ([Bigham, 1994; Jambor, 1994, 2003; Jambor and Blowes, 1998; Jambor et al., 2000](#)) identified many of the dominant mineral reaction products that form in sulfide-rich waste-rock and mill tailings. However, weathering processes in the low-temperature environment typical of mine wastes commonly result in the formation of intermixed secondary mineral phases that are extremely fine grained (nm to μm) and amorphous or poorly crystalline. A comprehensive understanding of the mineralogical complexity requires application of complementary micrometer- to nanometer-scale analytical techniques such as electron micro-analysis and imaging (SEM – scanning electron microscopy, EMPA – electron microprobe analysis, STEM – scanning transmission electron microscopy) and synchrotron-based methods including μ-XRF mapping and μ-XAFS (X-ray absorption fine structure, including X-ray absorption near edge structure – XANES and extended X-ray absorption fine structure – EXAFS). This approach allows identification of secondary-mineral assemblages across the appropriate scales which, in turn, informs questions of metal speciation, bioavailability and mobility of toxic metal (loid)s and long-term fate assessment ([Davis et al., 1993; Brown et al., 1999; Ostergren et al., 1999; Manceau et al., 2002; Hochella et al., 2005; Petrunic et al., 2006; Al et al., 2006; Keim and Markl, 2015; Mantha et al., 2019; Singer et al., 2020](#)).

The Faro Mine Complex (FMC, 62.36°N, 133.37°W, *SI Appendix*, [Fig. S1A](#)), located in south-central Yukon Territory, Canada, was operated from 1969 to 1998 for Zn and Pb extraction. After 30 years of mining operation and ore processing, waste materials stored at the site include 320 million tonnes of waste rock, 70 million tonnes of mill tailings, and low-grade ore stockpiles distributed over an area of 25 km^2. In this study we focus on developing a mechanistic understanding of the mineralogical controls on dissolved Pb concentrations in the effluent, specifically, oxidation of galena and the formation of secondary phases within the waste-rock pile.

2. Methods

2.1. Instrumentation, sample collection and analyses

Three boreholes (UW17-BH1, UW17-BH2, UW17-BH3) were completed in the waste-rock pile in July of 2017 ([Bao et al., 2020a, 2020b](#)). Double-side-polished thin sections (standard 30 μm) mounted with ethyl cyanoacrylate to Suprasil 2A Quartz glass were prepared by Spectrum Petrographics Inc. (Vancouver, WA) using freeze-dried waste-rock samples from discrete locations throughout the three borehole profiles. Altered grains of galena were identified on thin sections using optical microscopy and SEM/EDS analyses.

Long-term records of the chemistry (including pH, and dissolved Pb and Cu concentrations) of groundwater effluent from the groundwater capture and monitoring station SRK08-SPW3 (*SI Appendix*, [Fig. S1B](#))

located at the toe of the waste rock pile were retrieved from the site-wide hydrological, geochemical, and meteorological database EQuIS™, with access provided by the Canadian government department, Crown-Indigenous Relations and Northern Affairs Canada (CIRNAC).

2.2. EMPA analyses

Quantitative EMPA analyses, focused on altered galena grains, were conducted on carbon-coated thin sections using a JEOL 8230/8530 electron microprobe equipped with 5 tunable wavelength dispersive spectrometers (University of Ottawa). Analyses (Pb, S, Ag, Fe, Cu, Zn, Cd, Cr, Sb, As, Se, Al, Mn, Ni, Co, and Si) were first conducted at discrete points and along line transects on grains of galena and associated secondary-mineral coatings with the EMPA (1 μm beam and pixel size; 20 kV and 50 nA beam). To verify the stoichiometry of Pb and O on the secondary-mineral coatings, another line transect was conducted to analyze mass fractions of S, Pb, Fe, Cu, Sb, As, Al, Si, and O with the EMPA (15 kV and 20 nA). Carbon was included in these analyses, but the results are considered semi-quantitative. Analytical X-ray imaging was conducted to define spatial distributions of Pb, S, Cu, O, Fe, Zn, Si, Al, Sb, and As (20 kV and 20 nA, 1 μm beam and pixel size, acquisition time 100 ms/pixel). The O map was acquired using a LDE1 multilayer synthetic diffracting crystal. The following X-ray lines and standards were used for the analyses of points, line scans and X-ray maps: Pb Mα (galena), S Kα (pyrite or galena), Fe Kα (pyrite or marcasite), Ag Lα (Au60Ag40), Cu Kα (cubanite or cuprite), O Kα (crocoite), Zn Kα (sphalerite), Cd Lα (greenockite), Cr Kα (cochromite), Sb Lα (stibnite), As Lα (GaAs), Se Lα (Bi_2Se_3), Al Kα (chromite), Mn Kα (tephroite), Ni Kα (pentlandite), Co Kα (cochromite), and Si Kα (tephroite). Raw data corrections were conducted using a ZAF correction ([Armstrong, 1988](#)).

2.3. (S)TEM analyses

Extensively altered galena grain was the focus of detailed TEM analysis to characterize the nanoscale composition and mineralogy of the secondary coatings observed surrounding the altered galena. Following methods described by [Petrunic et al. (2006, 2009)](#), TEM foils (~10 μm × 30 μm), mounted on Cu support grids, were prepared in sections across the alteration rims of galena. The foils were prepared using Focused Ion Beam (Ga ion source) at Fibics Incorporated, Ottawa, ON. Annular Dark Field imaging (ADF) was conducted with a JEOL JEM-2100F (Materials Characterization Facility, University of Ottawa), and selected-area electron diffraction (SAED), electron-energy-loss spectroscopy (EELS), EDS analyses (EDAX Analyzer, DPP-II) and high-angle annular dark field imaging (HAADF) were conducted at the National Research Council of Canada on a FEI Titan 80–300 TEM equipped with a Gatan Tridiem 866 image filter and operated at 300 keV.

2.4. μ-XRF mapping and μ-XAFS measurements

Analytical μ-XRF images illustrating the spatial distribution of Pb, Cu and S, and μ-XANES spectra for the identification of Cu- and S-containing mineral phases, were collected on the Sector 20-ID-B and 13-ID-E beamlines at the Advanced Photon Source (APS), and at the soft X-ray microcharacterization beamline (SXRMB), Canadian Light Source (CLS). The thin sections were mounted to a sample holder at each beamline. At the APS Sector 20-ID-B beamline, the sample holder was maintained under air during analysis. The μ-XRF maps for Pb and Cu were acquired using a focused 2 μm × 2 μm beam (pixel size of 2 μm × 2 μm) and a four-element Vortex Si drift detector; the Pb and Cu fluorescence maps were collected simultaneously using a photon energy for excitation of 13500 eV (i.e. above the Pb L_{III} edge, and the Cu K edge). At the CLS SXRMB, the sample holder was inside a chamber that was maintained under vacuum. The μ-XRF map for Cu was acquired with an 8 μm × 8 μm beam (pixel size of 8 μm × 8 μm) and a 4-element silicon drift detector

(Bruker) using an excitation energy of 9000 eV. At the APS Sector 13-ID-E beamline, a sample holder was maintained in a He-gas filled environment. The μ-XRF map of S was acquired with a beam size of (1–2) μm × (1–2) μm (pixel size of 0.5 μm × 0.5 μm) using an excitation energy of 2490 eV (above the S K edge) and the measurements were made using a four-element Si Vortex Detector. At CLS SXRMB, Cu μ-XANES spectra were collected at spots that displayed elevated Cu concentration on the μ-XRF map. The Cu μ-XANES spectra were collected from 8959 to 9099 eV with step sizes of 0.45 eV near the Cu K-edge (8973–9009 eV, 6 s acquisition time per step), 2 eV between 8959 and 8973 eV and 0.75 eV between 9009 and 9099 eV (1 s acquisition time per step). At APS Sector 13-ID-E, S μ-XANES spectra were collected at 1 μm intervals along line transects that crossed from unaltered galena into the alteration rims. The S μ-XANES spectra were collected from 2442 to 2542 eV with a step size of 0.15 eV near the S K-edge (2465–2502 eV), 2 eV from 2442 to 2465 eV and 0.75 eV from 2502 to 2572 eV (1 s acquisition time per step in all energy regions).

Edge step normalization and background subtraction of μ-XANES spectra for S and Cu were conducted in Athena (Ravel and Newville, 2004). Linear combination fitting (LCF) was used to quantify the proportion of each S phase identified from the μ-XANES spectra, with components representing reference spectra for galena, covellite [CuS], marcasite [FeS$_2$], and melanterite [FeSO$_4$·7H$_2$O]. Reference spectra were collected at different beam times and on different beam lines: galena (Sector APS 13-ID-E), as well as marcasite, covellite, and melanterite (CLS SXRMB, Moncur et al., 2015; and obtained from SXRMB beamline scientist). All the reference spectra and the S μ-XANES spectra were calibrated to the sulfate peak energy of gypsum (2482.75 eV) for energy alignment between different beamlines. The fit quality of LCF results were evaluated with the R-factor values.

3. Results and Discussion

3.1. Field-scale geochemical characteristics in the waste-rock pile

Time-series records (2010–2020) for the water chemistry at the groundwater-capture and monitoring station SRK08-SPW3 (Fig. 1A) indicate that Pb concentrations range from 1.1 to 90 μg/L, with a trend toward higher concentrations over time. A similar increasing trend versus time is exhibited by Cu concentrations (4–167 μg/L) but the concentrations are generally higher than Pb by factors of 0.8–36.6, demonstrating a more rapid increase in Cu mobility in the weathered waste-rock pile. The increase in concentrations over time reflects the advancement of weathering and leaching processes in the waste-rock pile. The generally higher Cu concentrations relative to Pb are also manifest in the frequency histograms (Fig. 1B) for pH, and log-transformed concentrations of SO$_4$, Pb, and Cu from 120 pore-water samples extracted from the fine matrix of waste-rock samples collected from the surface and along depth profiles throughout the waste-rock pile (Bao et al., 2020b). These frequency histograms are asymmetric, and left-skewed for pH, slightly right-skewed for SO$_4$, and bimodal for Pb and Cu. The skewness for pH suggests that the majority of these water samples are alkaline, but with a long tail to extreme values as low as 1.4. Similarly, there are tails in the histograms that reach to elevated concentrations as high as 114,000 mg/L SO$_4$, 6.16 mg/L Pb and 277 mg/L Cu. Concentrations of dissolved Pb and Cu in these samples are pH-dependent (open squares in Fig. 1C), with a near-linear inverse correlation between pH and Cu, whereas the relationship between pH and Pb concentrations is more of a step function, with low Pb concentrations at pH > 7, and consistently elevated values at pH < 7. This non-linear trend for Pb concentrations versus pH probably reflects pH-dependent equilibrium between primary/secondary Pb-bearing phases and dissolved concentrations. The relationship between pH and Pb or Cu concentrations provides an indication of the potential evolution of the system as sulfide-mineral oxidation and associated acid-generation processes advance.
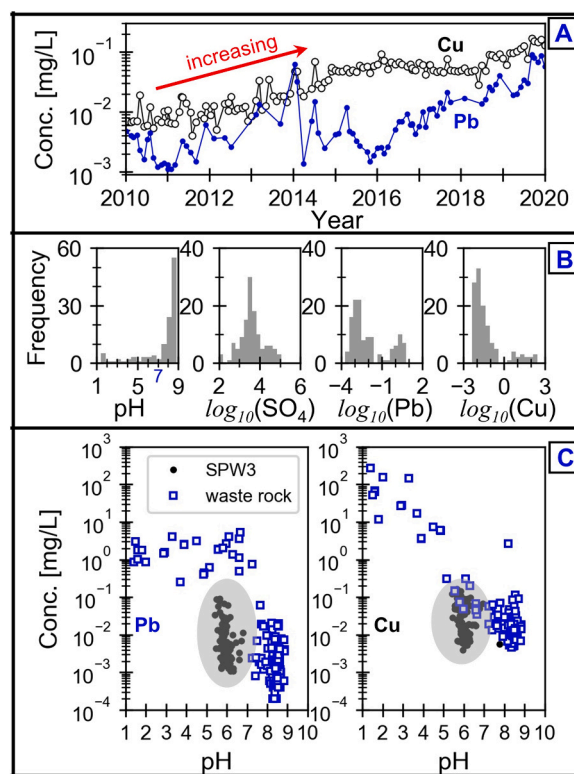

Fig. 1. (A) dissolved Pb and Cu concentrations in the effluent at the groundwater-capture and monitoring station SRK08-SPW3 (abbreviated as SPW3) from 2010 to 2020, (B) frequency histograms for pH, SO$_4$ (mg/L), Pb (mg/L) and Cu (mg/L) in 120 pore-water samples extracted from the fine matrix of the waste rock, (C) relationship between pH and Pb or Cu concentrations measured from waste-rock pore water and effluent-water samples. Data for pH, SO$_4$, Pb and Cu in waste-rock pore water are from Bao et al. (2020b).

3.2. Mesoscale depth profile and identification of altered grains of galena

Waste rock is usually deposited in benches via end dumping or push dumping, resulting in heterogeneous porous media with spatially variable mineralogy, particle size, sorting and water content (Amos et al., 2015). Detailed characterization of geochemical parameters in the waste-rock pile has been conducted within the framework of the spatial heterogeneity (Bao et al., 2020b). Integrated depth profiles (Fig. 2) of solid-phase and dissolved Pb and Cu concentrations, pore-gas O$_2$ concentration, pore-water pH and temperature from one borehole location (UW17-BH2, *SI Appendix*, Fig. S1B) illustrate the relationships among these parameters. Representative profiles of temperature on November 1, 2017 (winter) and July 1, 2018 (summer) display seasonal variation near the surface (< 9 mbgs) but the profiles at greater depths are unchanging over time. A quasi-diffusion profile for O$_2$ concentration was observed, decreasing from atmospheric concentrations near the surface to 1.5 vol% at 58.6 mbgs. The borehole is located centrally within the waste-rock pile (*SI Appendix*, Fig. S1B), where vertical pore-gas transport may be constrained by diffusion in the absence of strong gas advection. However, the O$_2$ concentration rebounded near the bottom of the waste rock, likely reflecting thermally driven gas advection occurring along the base (Harries and Ritchie, 1985; Lefebvre et al., 2001a, 2001b; Bao et al., 2020b). Similar patterns in the depth profiles of Pb and Cu concentrations, both in aqueous and solid phases, suggest releases of Pb and Cu from the solid phase due to ongoing mineral oxidation. The concentration of O$_2$ is significantly depleted by sulfide oxidation at depths between 30 and 40 m depth where there are elevated solid-phase concentrations of Pb, Cu, S, Fe and Zn, resulting in acidic pH, relatively high concentrations of dissolved Pb and Cu, and elevated temperature (Fig. 2; Bao et al., 2020b). These characteristics indicate an active zone of
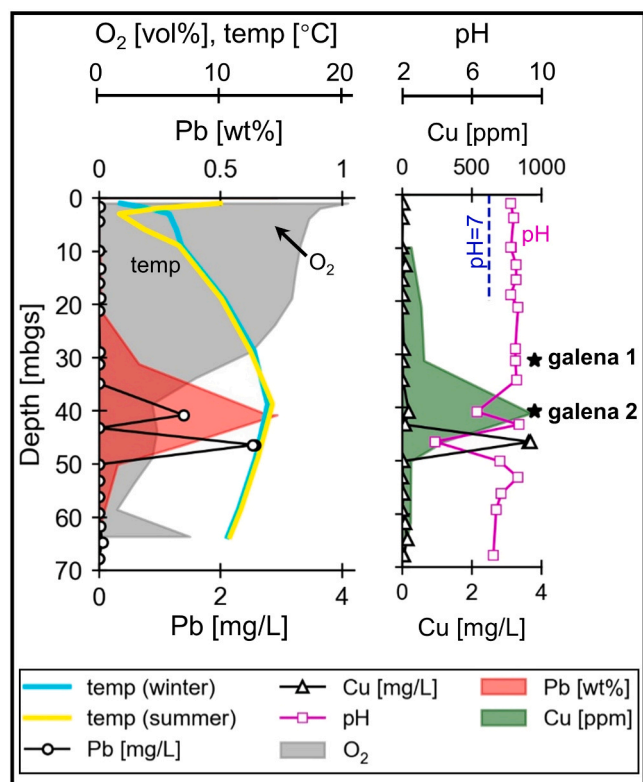
Fig. 2. Temperature and geochemical conditions in one waste-rock borehole profile (data integrated from Bao et al., 2020a; 2020b) including the locations of two representative altered galena grains (galena 1 collected at 31.2 mbgs – meter below ground surface, and galena 2 collected at 40.8 mbgs). Aqueous- and solid-phase concentrations of Pb and Cu are represented by the open black circles and triangles and by the shaded red and green zones, respectively. Note, the bottom of the waste rock is located at 65.8 mbgs in this borehole location.

sulfide-mineral oxidation. In the neutral-pH region of this zone, extensively oxidized micron-scale grains of galena were observed (*SI Appendix*, Table S2) with alteration rims ranging from 1 to 30 μm thick (Fig. 3). Galena grains with weak alteration rims were also detected where the pH is acidic.

3.3. Investigations of galena oxidation

3.3.1. Micrometer-scale EMPA, μ-XRF and μ-XAFS analyses

The alteration rims surrounding galena are clearly evident from optical microscopy and BSE images (Fig. 3). EMPA elemental maps of galena 1 for Pb, S and O, and in the tri-color map of Cu, Pb and S distributions, indicate that the alteration rims are primarily composed of Pb oxide, oxyhydroxide or carbonate (Fig. 4). The EMPA analyses along the line transect L2 (Fig. 4A) indicate that the Pb-rich secondary precipitates are primarily composed of Pb, C and O (*SI Appendix*, Fig. S2). The C analyses are semi-quantitative, but the Pb:O stoichiometry is 1:3, consistent with a Pb-carbonate such as cerussite (Fig. 4B, and also refer to *SI Appendix*, Table S3 for weight and estimated mole fractions of Pb, S, Cu, C and O). The X-ray maps also reveal the presence of a thin (< 5 μm) Cu-rich zone directly adjacent to the galena and discontinuous enrichment of Fe in the outer margins of the alteration rims. Line transects plotted versus distance from the galena to the exterior margin (Fig. 4B, and *SI Appendix*, Fig. S3) demonstrate a decline in Pb concentration. Peaks in the Cu concentration profiles occur at the interface with galena, indicating secondary Cu accumulation at the oxidation interface. There are trace to minor amounts of Cu (0.05–0.15 wt%, *SI Appendix*, Table S3) present in galena. Mass balance calculations suggest that there is 20 times more Cu in the alteration rims than that in the un-oxidized portion of the galena grain. Along with the high concentrations observed in the pore water (Fig. 2), Cu enrichment along the alteration rims suggest that the pore water is the dominant source for Cu that accumulates at the interface.

Spatial distributions of Pb, Cu, and S from EMPA elemental X-ray maps (Fig. 4) are consistent with μ-XRF maps (Fig. 5). The close match between Cu μ-XANES spectra (Fig. 5C) and a covellite standard (Buis, 2016) indicates that the Cu-S phase at the interface between galena and the surrounding alteration rims is covellite. This is also consistent with the EMPA analyses along the line transect L2 (Fig. 4B) that a 1:1 atomic ratio for Cu and S is necessary for reconciling the data with a mixture of galena, cerussite and covellite at the interface. The normalized S K-edge μ-XANES spectra along the line transect (Fig. 5D, E) and the reference spectra of galena, covellite, marcasite, and melanterite show well-defined absorption edges. Comparison of the S K-edge μ-XANES spectra and the reference spectra (Fig. 5E, and *SI Appendix*, Fig. S4), as well as the element composition (Fig. 4) suggest the main peak at 2471–2473 eV corresponds to sulfides (i.e. marcasite, covellite, and
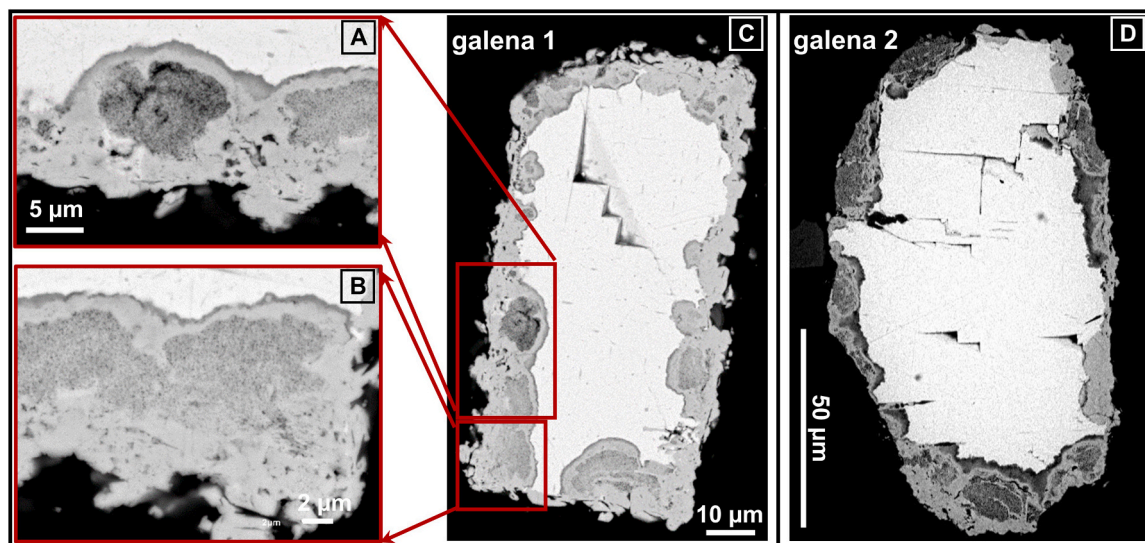

Fig. 3. Backscattered electron (BSE) images of altered galena grains. Galena 1 and galena 2 (locations shown in Fig. 2) were chosen as representative grains to characterize the extent and degree of galena oxidation, mechanism of Pb release, and the nature of secondary phases. Pore-water and solid-phase geochemical parameters at locations of galena 1 and 2 are summarized in *SI Appendix,* Table S2. Both grains are located in a neutral pH pore-water environment.
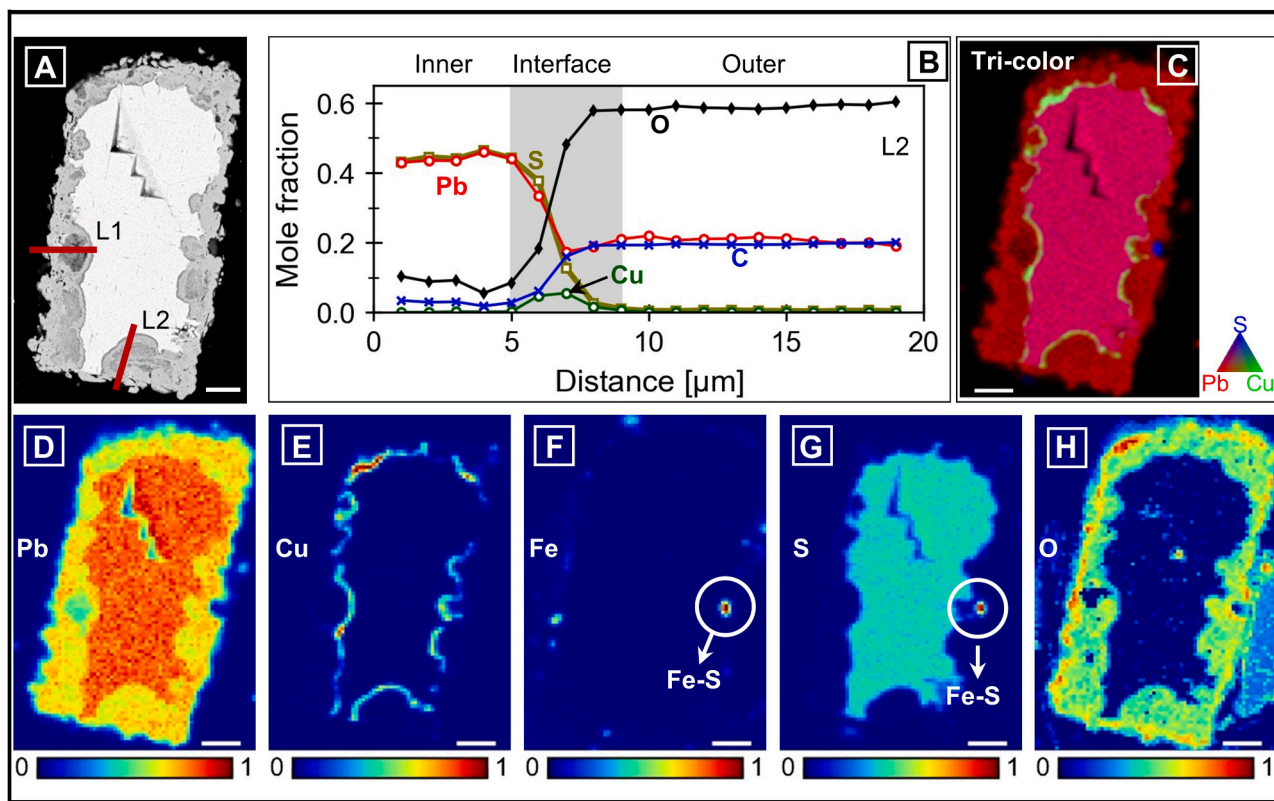
Fig. 4. EMPA data for an altered mineral grain, galena 1: (A) BSE image showing the locations of analytical line transects L1 and L2. (B) Analytical data (mole fractions) for Pb, S, Cu, O and C along the line transect L2. The C analyses are semi-quantitative (see raw data and estimated mole fractions in *SI Appendix* Fig. S2 and Table S3). (C) Tri-color map for Pb (red), Cu (green) and S (blue). Discrete elemental maps for (D) Pb, (E) Cu, (F) Fe, (G) S, and (H) O. The white scale bars represent 10 μm.
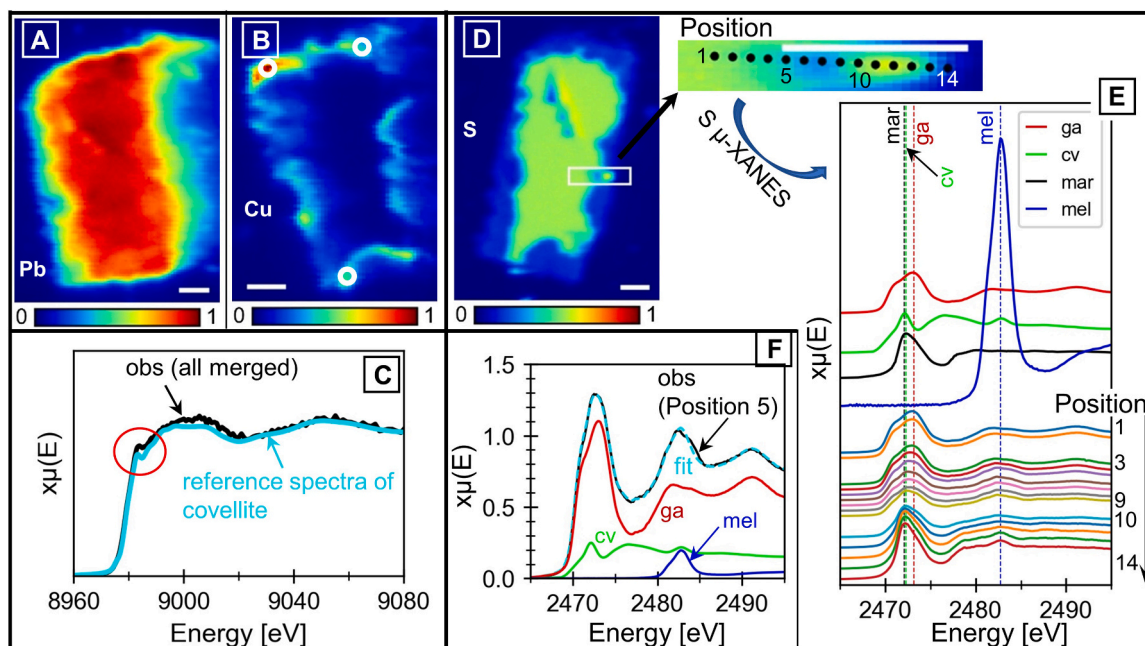

Fig. 5. Synchrotron-based μ-XRF mapping and μ-XANES measurements for an altered mineral grain, galena 1: the μ-XRF maps of Pb (A) and Cu (B) were acquired at APS Sector 20-ID-B beamline. (C) Copper μ-XANES spectra were collected at three spots with 3–5 scans per spot at CLS SXRMB. The approximate locations are shown as white open circles in subplot B. The black solid line represents measured data (combination of μ-XANES spectra collected at three spots), and the cyan solid line represents the Cu XANES for a covellite standard. (D) The μ-XRF map for S was acquired at APS Sector 13-ID-E beamline. (E) Sulfur K-edge μ-XANES spectra collected from 1 μm spaced points along the line transect of 14 μm, and reference spectra of galena (ga), covellite (cv), marcasite (mar), and melanterite (mel). (F) LCF analysis for the S K-edge μ-XANES spectra at Position 5 with three fit components of the reference spectra. The white scale bars represent 10 μm.

galena) and the peak at 2482.75 eV corresponds to sulfate. It should be noted that marcasite is chosen as a representative for the Fe-S particle, and melanterite is chosen as a representative of sulfate. The galena and covellite peaks are most intense for pixels on the line transect near the surface of galena, and the marcasite peak is most intense on the Fe-S particle (*SI Appendix*, Fig. S4). LCF analysis was used to estimate the fractions of S phases at every pixel along the line transect over an energy range of 2465–2495 eV, with an example of fitted spectra using LCF at Position 5 shown in Fig. 5F. Combinations of galena, covellite, marcasite and melanterite can describe the spectra collected at each pixel along the line transect. A summary of the fitted percentage for each reference compound is provided in Table 1. Along the line transect from galena toward the exterior edge, a depletion trend in the fractions of galena and an enrichment of covellite at the interface are observed. The Fe-S particle is mainly composed of marcasite, however, it is uncertain whether this Fe-S particle is an inclusion or a secondary phase. A minor amount of sulfate (1–3%) is also present on the alteration rims. In general, multiple S phases may be present on the altered grain of galena, and some S was sequestered as covellite. However, a rapid depletion of S on the alteration rims over the entire galena grain (Figs. 4G and 5D, and *SI Appendix*, Table S3) likely indicates that the majority of the S was oxidized to sulfate and released to the pore water.

3.3.2. Nanometer-scale TEM investigation

The BSE image of galena 2 (Fig. 3D and 6A) has distinct zones with differing gray-scale intensities reflecting the changes in composition: the bright central zone containing triangular cleavage pits (i.e. characteristic of cubic crystal structure) represents galena; there is a thin, dark, somewhat discontinuous zone along the interface between galena and the alteration rims; and the remainder of the alteration rims is mostly light gray with some discontinuous medium-gray layers. These zones in the alteration rims were the focus of a nano-scale investigation using analytical (S)TEM. Electron-transparent sections were prepared by FIB across two regions of interest (ROI-A and ROI-B; Fig. 6A). Despite the complexity of the grey-scale intensities in the alteration rims, which suggest a corresponding change in secondary mineralogy, the (S)TEM investigations identify only three secondary mineral components. Consistent with observations from the EMPA elemental maps and

analyses, a Cu-S phase, identified by μ-XANES as covellite occurs as a thin (< 5 μm) layer at the interface between galena and the Pb-C-O alteration product which forms the bulk of the alteration rims (Fig. 6B, and more details of EMPA data in *SI Appendix*, Fig. S6). In some locations, covellite occurs as ~500 nm thick bands interlayered with the Pb-C-O material near the surface of galena (Fig. 6F, G), and it is also observed forming very thin veins that line the walls of nano-scale fractures in galena (Fig. 6H, I). The contemporaneous STEM EDS/EELS analyses display distinct Cu-S and Pb-O signals as the beam crosses the interface (Fig. 6C). Although carbon was not determined in these analyses, the data are consistent with that from the EMPA, indicating that the alteration rims are primarily comprised of Pb, C and O. The Pb-C-O phase has a mottled and porous appearance that results from the aggregation of roughly spherical particles with diameters < 100 nm (Fig. 6B, D). In Fig. 6E, EELS spectra collected along a transect (Fig. 6D) are compared to a reference spectrum for oxidized Pb foil (Gatan EELS Atlas; Pb0-3890 eV), demonstrating a very close match. The identity of the Pb-C-O phase was further investigated using selected-area electron diffraction. The d-spacings obtained from SAED patterns on the Pb-C-O phase (Fig. 7, and Table 2) indicate that the Pb-C-O material is dominantly comprised of cerussite (clearly evidenced by the intensity of 011 diffraction line) and a possible minor phase of shannonite ($Pb_2O(CO_3)$).

3.4. Galena oxidation and its influence on Pb mobility

Secondary minerals are ubiquitous in mine wastes and they form as a result of the oxidative weathering of primary sulfide minerals and interactions with carbonate and aluminosilicate gangue minerals. The solubility of secondary minerals is commonly pH-dependent; as pH varies through time in response to changing rates of sulfide oxidation, acid neutralization and the stability of secondary minerals. The formation and dissolution of secondary precipitates control the aqueous concentration and mobility of metal(loid)s. Therefore, definitive identification of secondary phases provides valuable information for assessing the storage, release and transport of metal(loids) in minewaste systems. Previous work has demonstrated that secondary minerals formed during galena oxidation include lead hydroxide, lead oxide, anglesite, cerussite, and other Pb-bearing carbonate or oxyhydroxide phases (Buckley and Woods, 1984; Davis et al., 1993; Fornasiero et al., 1994; Lin, 1997; Jamieson, 2011; Lara et al., 2011; Blowes et al., 2014; Keim and Markl, 2015). Similarly, it has been shown that secondary Cu sulfides, such as covellite [CuS] and chalcocite [Cu_2S] form on the surfaces of pyrrhotite (Blowes and Jambor, 1990; Holmström et al., 1999), arsenopyrite (Petrunic et al., 2006), chalcopyrite (Dold and Fontbote, 2001), and sphalerite (Boorman and Watson, 1976; Petrunic et al., 2009) in tailing impoundments via replacement reactions driven by solubility differences.

Secondary minerals commonly form as a result of incongruent dissolution processes, creating coatings on pre-existing phases that were rendered unstable under the oxidizing conditions of the waste-rock pile. As a consequence, they exist as nano- to micro-scale features and rigorous studies of their physical and chemical properties must employ techniques that are effective at that scale. The question of whether the results of nano- and micro-scale investigations are representative at larger scales is important if, as in this study, the results may factor into decision making for reclamation planning. Detailed studies on the large numbers of samples would be required to demonstrate that the results are statistically representative over large areas or volumes. However, we rely on knowledge of the systematic controls on mineral stability. Specifically, it is well known that pH, redox conditions, temperature and solution composition are fundamental determinants of mineral stability in mine-waste systems. Conducting studies across scales, such that measurements of geochemical parameters at relatively large scale (10–1000 s of meters), can be invoked to infer the spatial relevance of the nano- and micro-scale data. In this case, aqueous-, solid- and gas-phase geochemical data, along with temperature measurements,
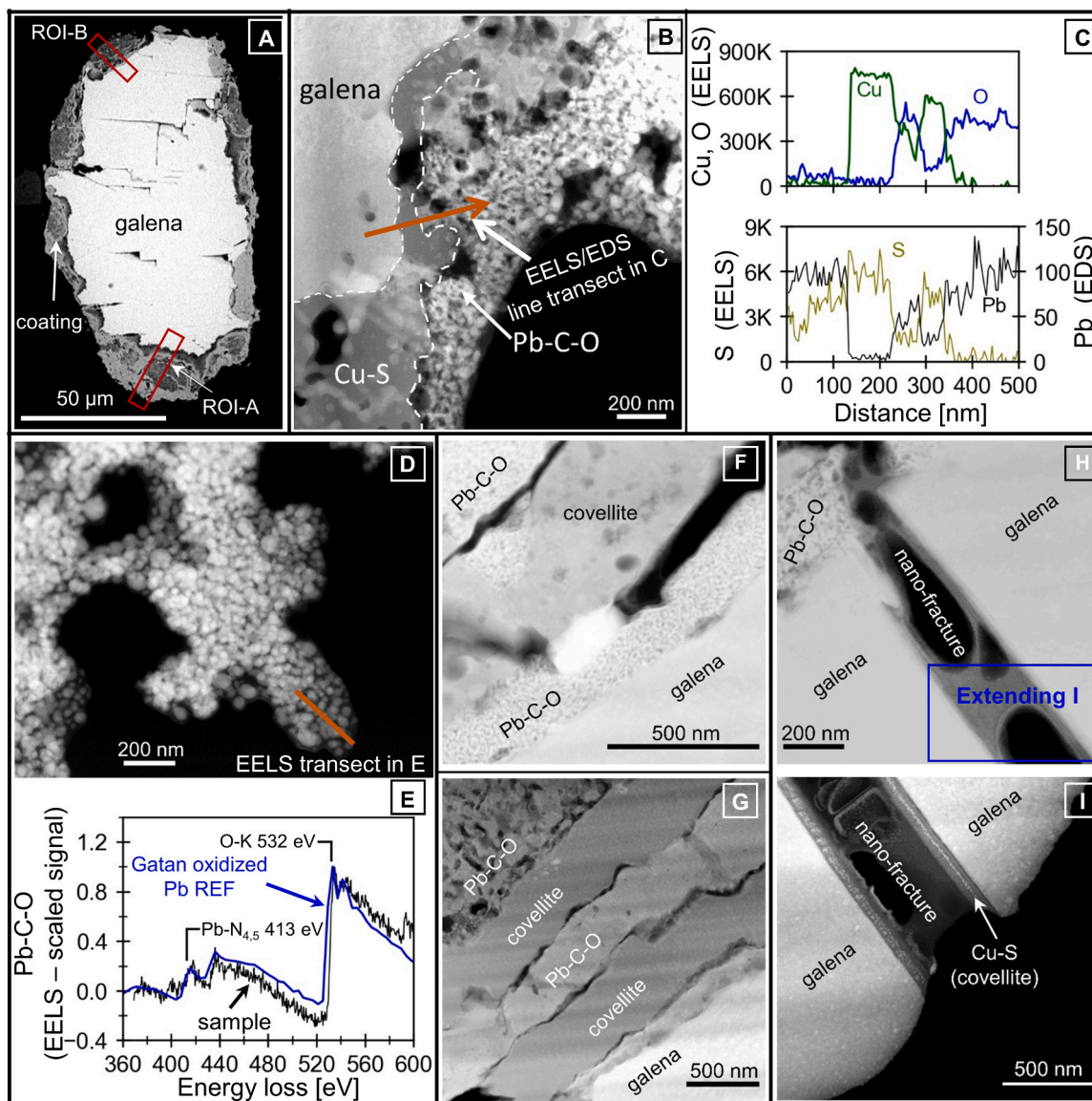
Table 1

Distribution of S phases based on LCF of S K-edge μ-XANES spectra along the line transect in Fig. 5D.

Position	Percentage of S phases from the μ-XANES spectra				R-factor
	Galena	Covellite	Marcasite	Melanterite	
1	100.0%	–	–	–	2.2×10^{-4}
2	95.7%	4.3%	–	–	1.3×10^{-4}
3	91.4%	8.6%	–	–	4.0×10^{-4}
4	86.9%	12.0%	–	1.1%	4.4×10^{-4}
5	79.3%	18.6%	–	2.1%	2.8×10^{-4}
6	77.7%	19.9%	–	2.4%	4.7×10^{-4}
7	67.5%	18.3%	11.0%	3.2%	7.1×10^{-4}
8	66.5%	14.8%	15.2%	3.4%	1.2×10^{-3}
9	56.8%	9.7%	30.5%	3.0%	1.1×10^{-3}
10	36.5%	–	61.8%	1.7%	1.4×10^{-3}
11	25.9%	–	72.7%	1.4%	1.7×10^{-3}
12	17.6%	–	81.2%	1.2%	1.9×10^{-3}
13	11.9%	–	86.6%	1.5%	2.4×10^{-3}
14	5.7%	–	92.9%	1.4%	2.2×10^{-3}

The S K-edge μ-XANES spectra along the line transect were collected at 1 μm interval (beam spot size of 1–2 μm). The estimated fractions of S phases also reflect the information from nearby areas within the beam area.

The maximum number of reference-spectra components used for the LCF analysis was limited to 4. Sensitivity analysis was applied to evaluate the presence of any S phases with estimated ratios < 5% (i.e. sulfate). Sulfate accounts for a minor fraction. However, its presence can significantly influence the fit criteria R-factor values (> 100%, with an example given at Position 5 in *SI Appendix*, Fig. S5), and thus the minor mass of sulfate cannot be removed from the fit.

Fig. 6. (A) BSE image of an altered galena grain, galena 2 with two rectangles representing locations ROI-A and ROI-B where foils used for (S) TEM analyses were prepared by sectioning with a FIB. (B) STEM HAADF image of galena, Cu-S phase and Pb-C-O phase, showing the location for the simultaneous EELS/EDS analytical transect shown in the subplot C. (C) EELS data for O, S and Cu and EDS data for Pb along the line transect. The line transect was collected in the direction indicated by the orange arrow. The units of the vertical axes are in counts. (D) STEM HAADF image of nano-structured Pb-C-O phase in the alteration rims, showing the location of an EELS line profile. (E) A representative EELS spectrum from the profile is compared to a reference spectrum for Pb oxide. The units of the vertical axis are normalized counts. (F) STEM ADF image of covellite intergrown with Pb-C-O material, i.e. cerussite and shannonite. (G) STEM ADF image of interlayered covellite and Pb-C-O material. (H and I) STEM ADF images of internal nano-fracture in galena with covellite (a Cu-S phase) on the walls.

indicate that the galena alteration features observed in this study occur in neutral-pH zones that are undergoing active sulfide oxidation (Fig. 2). Altered galena grains collected from zones with similar geochemical properties approximately 10 m show similar alteration patterns, suggesting that this rationale is appropriate.

In this study, the STEM EELS/EDS and µ-XANES analyses indicate that aqueous Cu precipitated as covellite on the surface of galena undergoing dissolution which can be represented in part by the following reaction:

$$PbS + Cu^{2+} \rightarrow Pb^{2+} + CuS \tag{1}$$

Lead (II) ions released by this reaction, or by oxidation of galena in a neutral-pH pore-water environment, may react with dissolved inorganic carbon species to precipitate as Pb-bearing carbonates such as cerussite:

$$Pb^{2+} + HCO_3^- \rightarrow PbCO_3 + H^+ \tag{2}$$

In this case cerussite is the dominant compound and shannonite is a possible minor phase on the alteration rims of galena grains. At the galena surface, secondary covellite and Pb-bearing carbonates are intergrown (STEM ADF images in Fig. 6F, G), likely indicating the concurrent occurrence of galena oxidation and secondary precipitation of covellite and Pb-bearing carbonates in the waste-rock environment. However, equilibrium calculation of bulk pore-water geochemistry using the geochemical model PHREEQC (Parkhurst and Appelo, 2013) with the water4f database (Ball and Nordstrom, 1991) predicts undersaturation of cerussite in the pore water (saturation indices < 0) at both locations. This discrepancy suggests that bulk aqueous geochemical measurements, combined with thermodynamic predictions of precipitation and dissolution, without micro- and nano-scale observations may not adequately represent the local mineralogical evolution, as was discussed in other studies (Hochella Jr et al., 1999; Petrunic and Al, 2005).

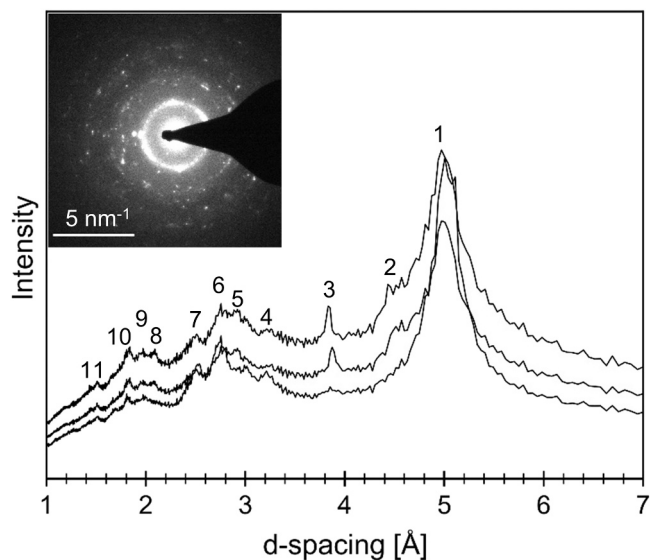Characterization of geochemical heterogeneity in the waste-rock pile

Fig. 7. Electron diffraction patterns derived by radial integration of the image intensity from the selected-area electron-diffraction patterns collected on the Pb-C-O material (example shown in the upper left). All diffraction lines except 2 and 3 (unidentified) correspond to cerussite and/or shannonite (Table 2).

Table 2
Identification and indexing of electron diffraction lines obtained from the Pb-C-O material.

Diffraction line	Measured d-spacing (Å)		Phase[a,b,c]	Index (h k l)	
	d-spacing peak	d-spacing range		Cerussite	Shannonite
1	4.97	4.90–5.10	cerussite	011	
2	4.57	4.48–4.57	?		
3	3.87	3.83–3.91	?		
4	3.21	3.17–3.24	shannonite		022/112/121
5	2.93	2.92–2.94	shannonite		013
6	2.76	2.70–2.80	shannonite		122
7	2.51	2.49–2.52	cerussite/shannonite	112/022/130	131
8	2.08	2.06–2.10	cerussite/shannonite	221	114
9	1.97	1.96–2.00	cerussite/shannonite	202	203
10	1.82	1.80–1.86	cerussite/shannonite	113/023	034/043/223/232
11	1.52	1.50–1.54	cerussite/shannonite	004/223	322/135

[a] Colby and Lacoste (1933).
[b] Krivovichev and Burns (2000).
[c] Antao and Hassan (2009).

illustrates the development of acidic pore water (pH as low as 1.4; Fig. 1B, and Bao et al., 2020b), particularly at mid depth in the profile (Fig. 2). The secondary cerussite and shannonite phases were only encountered in a neutral-pH pore-water environment. The mineralogical investigation only detected weak alteration rims on small amount of galena grains in the zones of acidic pH where secondary anglesite precipitation might be expected. The solubility of shannonite is not known. But cerussite solubility is pH-dependent and very low under neutral-pH, carbonate rich conditions (*SI Appendix*, Table S1), leading to the pH-dependence of Pb concentrations (Fig. 1C and Fig. 2; *SI Appendix*, Table S2). In the event of a pH decrease, there will be a tendency for dissolution of cerussite, potentially leading to higher concentrations of Pb in water leaching from the waste-rock pile (Fig. 1C; current

maximum observed Pb concentration of 6.16 mg/L, Bao et al., 2020b). In the absence of remedial actions, water infiltration and O_2 ingress into the waste-rock pile will remain unimpeded, and sustained oxidation of sulfide minerals will continue to provide a source of Pb and other metals and contribute to long-term leaching and elevated concentrations in the effluent (Fig. 1A).

4. Conclusions and Implications

The combination of cross-scale measurements ranging from field-scale parameters to mm- to nm-scale analytical investigations allows for the delineation of metal storage and release mechanisms, and aids in the evaluation of the potential release of metals from mine wastes to the natural environment. Here we focused on a waste-rock pile that contains a highly variable S content, present in the form of multiple sulfide-bearing minerals (including pyrite, sphalerite, galena, pyrrhotite, and chalcopyrite, Bao et al., 2020b) with the specific goals of understanding the mechanisms of galena oxidation and the subsequent impact of secondary-mineral phases that retain and limit the mobility of Pb and other metals. The results show that, under the near-neutral pH conditions prevalent in the locations where the galena grains were collected, dissolved Cu was partially sequestered by the formation of covellite on the surface of galena, Pb was largely retained as secondary Pb-bearing carbonates (i.e. cerussite), and the majority of S was fully oxidized to sulfate and released to the pore water. However, the physical, mineralogical and geochemical conditions that control secondary-mineral stability are transient (e.g. the pH and other geochemical conditions in waste rock can change over time). Sustained oxidation of iron-sulfide minerals (e.g. pyrrhotite and pyrite) will continue to acidify the pore water, potentially leading to the dissolution of secondary cerussite and mobilization of dissolved Pb. Efforts toward safe, long-term management of mine-waste materials must account for these processes. Reclamation efforts should begin with a thorough quantitative representation of the important physical, mineralogical and chemical characteristics and a comprehensive understanding of the processes, at the macro, micro and nano scales, that control the evolution of mine-waste systems. Integrating the complex interactions among the physical and chemical processes, using a numerical modeling framework allows simulations of the system evolution over the long term. Incremental improvements in the knowledge of geochemical conditions, and the corresponding nanometer- and micrometer-scale mineralogical properties, are required to refine conceptual and numerical models. The present study investigating the mechanisms of galena oxidation and secondary phase precipitation is an example of such an incremental advancement illustrating the spatial heterogeneity of secondary phases at micro and nano scales, that can contribute to improved models and a better understanding of the storage and release of metal(loid)s in mine wastes.

CRediT authorship contribution statement

Zhongwen Bao: Conceptualization, Methodology, (S)TEM analyses, EMPA analyses, synchrotron measurements, field investigation and laboratory analyses, data collection and analyses, and original draft preparation, data analyses and paper writing. **Tom Al**: Conceptualization, Methodology, (S)TEM analyses, Supervision, and funding, data analyses and paper writing. **Martin Couillard**: (S)TEM analyses, Investigation. **Glenn Poirier**: EMPA analyses, Investigation. **Jeff Bain**: field investigation and laboratory analyses. **Heather K. Shrimpton**: synchrotron measurements, Investigation. **Y. Zou Finfrock**: synchrotron measurements, Investigation. **Antonio Lanzirotti**: synchrotron measurements, Investigation. **Dogan Paktunc**: Conceptualization, Methodology, data analyses and paper writing. **Emily Saurette**: synchrotron measurements, Investigation. **Yongfeng Hu**: synchrotron measurements, Investigation. **Carol J. Ptacek**: Supervision, and funding. **David W. Blowes**: Conceptualization, Methodology, Supervision, and funding, data analyses and paper writing. All the coauthors reviewed and edited

the paper.

Declaration of Competing Interest

The authors declare that they have no known competing financial interests or personal relationships that could have appeared to influence the work reported in this paper.

Acknowledgments

Appendix A. Supporting information

Supplementary data associated with this article can be found in the online version at doi:10.1016/j.jhazmat.2021.125130.

References

Al, T.A., Leybourne, M.I., Maprani, A.C., MacQuarrie, K.T., Dalziel, J.A., Fox, D., Yeats, P.A., 2006. Effects of acid-sulfate weathering and cyanide-containing gold tailings on the transport and fate of mercury and other metals in Gossan Creek: Murray Brook mine, New Brunswick, Canada. Appl. Geochem. 21, 1969–1985.

Amos, R.T., Blowes, D.W., Bailey, B.L., Sego, D.C., Smith, L., Ritchie, A.I.M., 2015. Waste-rock hydrogeology and geochemistry. Appl. Geochem. 57, 140–156.

Antao, S.M., Hassan, I., 2009. The orthorhombic structure of CaCO₃, SrCO₃, PbCO₃ and BaCO₃: linear structural trends. Can. Mineral. 47 (5), 1245–1255.

Armstrong, J.T., 1988. Quantitative analysis of silicates and oxide minerals: comparison of Monte-Carlo, ZAF and Phi-Rho-Z procedures. Microbe Anal. 239–246.

Badawy, S.H., Helal, M.I.D., Chaudri, A.M., Lawlor, K., McGrath, S.P., 2002. Soil solid-phase controls lead activity in soil solution. J. Environ. Qual. 31, 162–167.

Ball, J.W., Nordstrom, D.K., 1991. User Manual for WATQF4 with Revised Thermal Dynamic Database and Test Cases for Calculating Speciation of Major, Trace, and Redox Elements in Natural Waters. USGS, pp. 91–183. Open-file report.

Bao, Z., Blowes, D.W., Ptacek, C.J., Bain, J., Holland, S.P., Wilson, D., Wilson, W., Mackenzie, P., 2020a. Faro Waste Rock Project: Characterizing variably saturated flow behavior through full-scale waste-rock dumps in the continental subarctic region of Northern Canada using field measurements and stable isotopes of water. Water Resour. Res. 56 e2019WR026374.

Bao, Z., Bain, J., Holland, S.P., Wilson, D., MacKenize, P., Ptacek, C.J., Blowes, D.W., 2020b. Faro Waste Rock Project: Characterizing geochemical heterogeneity in sulfide- and carbonate-rich waste rock. Appl. Geochem. 121, 104691.

Bigham, J.M., 1994. Mineralogy of ochre deposits formed by sulfide oxidation. In: Jambor, J.L., Blowes, D.W. (Eds.), Short Course Handbook on Environmental Geochemistry of Sulfide Mine-Wastes. Mineralogical Association of Canada, pp. 103–132.

Blowes, D.W., Jambor, J.L., 1990. The pore-water geochemistry and the mineralogy of the vadose zone of sulfide tailings, Waite Amulet, Quebec, Canada. Appl. Geochem. 5, 327–346.

Blowes, D.W., Ptacek, C.J., Jambor, J.L., Weisener, C.G., Paktunc, D., Gould, W.D., Johnson, D.B., 2014. 11.5 - The Geochemistry of ACID MINE Drainage. In: Holland, H.D., Turekian, K.K. (Eds.), Treatise on Geochemistry, second ed., 2014. Elsevier, Oxford, pp. 131–190.

Boorman, R.S., Watson, D.M., 1976. Chemical processes in abandoned sulphide tailings dumps and environmental implications for northeastern New Brunswick. Can. Inst. Min. Metall. Bull. 69, 86–96.

Buckley, A.N., Woods, R., 1984. An X-ray photoelectron spectroscopic study of the oxidation of galena. Appl. Surf. Sci. 17 (4), 401–414.

Buis, J.R., 2016. Copper isotope fractionation and the evolution of sulfide alteration in a Sudbury tailings impoundment. University of Waterloo. Master's thesis.

Brown Jr., G.E., Foster, A.L., Ostergren, J.D., 1999. Mineral surfaces and bioavailability of heavy metals: A molecular-scale perspective. Proc. Natl. Acad. Sci. USA 96, 3388–3395.

Cheng, H., Hu, Y., 2010. Lead (Pb) isotopic fingerprinting and its applications in lead pollution studies in China: a review. Environ. Pollut. 158, 1134–1146.

Colby, M., LaCoste, L., 1933. The crystal structure of cerussite. Z. Kristallogr. 84, 299–309.

Davis, A., Drexler, J.W., Ruby, M.V., Nicholson, A., 1993. Micromineralogy of mine wastes in relation to lead bioavailability, Butte, Montana. Environ. Sci. Technol. 27, 1415–1425.

Dold, B., Fontbote, L., 2001. Element cycling and secondary mineralogy in porphyry copper tailings as a function of climate, primary mineralogy, and mineral processing. J. Geochem. Explor. 74, 3–55.

Fornasiero, D., Li, F., Ralston, J., Smart, R.S.C., 1994. Oxidation of galena surfaces: I. X-ray photoelectron spectroscopic and dissolution kinetics studies. J. Colloid Interface Sci. 164 (2), 333–344.

Harries, J.R., Ritchie, A.I.M., 1985. Pore gas composition in waste rock dumps undergoing pyritic oxidation. Soil Sci. 140 (2), 143–152.

Hochella Jr., M.F., Moore, J.N., Putnis, C.V., Putnis, A., Kasama, T., Eberl, D.D., 2005. Direct observation of heavy metal mineral association from the Clark Fork River Superfund Complex: implications for metal transport and bioavailability. Geochim. Cosmochim. Ac. 69, 1651–1663.

Hochella Jr., M.F., Moore, J.N., Golla, U., Putnis, A., 1999. A TEM study of samples from acid mine drainage systems: metal-mineral association with implications for transport. Geochim. Cosmochim. Ac. 63 (19–20), 3395–3406.

Holmström, H., Ljungberg, J., Ekström, M., Öhlander, B., 1999. Secondary copper enrichment in tailings at the Laver mine, northern Sweden. Environ. Geol. 38 (4), 327–342.

Hudson-Edwards, K.A., Jamieson, H.E., Lottermoser, B.G., 2011. Mine wastes: past, present, future. Elements 7, 375–380.

Jambor, J.L., 1994. Mineralogy of sulfide-rich tailings and their alteration products. In: Jambor, J.L., Blowes, D.W. (Eds.), The Environmental Geochemistry of Sulfide Mine-wastes, vol. 22. Mineralogical Association of Canada, pp. 59–102.

Jambor, J.L., 2003. Mine-waste mineralogy and mineralogical perspectives of acid—base accounting. In: Jambor, J.L., Blowes, D.W., Ritchie, A.I.M. (Eds.), Environmental Aspects of Mine Wastes, vol. 31. Mineralogical Association of Canada, pp. 117–145.

Jambor, J.L., Blowes, D.W., 1998. Theory and applications of mineralogy in environmental studies of sulfide-bearing mine wastes. In: Cabri, L.J., Vaughan, D.J. (Eds.), Modern Approaches to Ore and Environmental Mineralogy, vol. 27. Mineralogical Association of Canada, pp. 367–401.

Jambor, J.L., Nordstrom, D.K., Alpers, C.N., 2000. Metal-sulfate salts from sulfide mineral oxidation. Rev. Mineral. Geochem. 40 (1), 305–350.

Jamieson, H.E., 2011. Geochemistry and mineralogy of solid mine waste: essential knowledge for predicting environmental impact. Elements 7, 381–386.

Keim, M.F., Markl, G., 2015. Weathering of galena: Mineralogical processes, hydrogeochemical fluid path modeling, and estimation of the growth rate of pyromorphite. Am. Mineral. 100, 1584–1594.

Krivovichev, S., Burns, P., 2000. Crystal chemistry of basic lead carbonates. I. Crystal structure of synthetic shannonite, Pb₂O(CO₃). Mineral. Mag. 64, 1063–1068.

Lefebvre, R., Hockley, D., Smolensky, J., Gélinas, P., 2001a. Multiphase transfer processes in waste rock piles producing acid mine drainage: 1: conceptual model and system characterization. J. Contam. Hydrol. 52, 137–164.

Lefebvre, R., Hockley, D., Smolensky, J., Lamontagne, A., 2001b. Multiphase transfer processes in waste rock piles producing acid mine drainage: 2. Applications of numerical simulation. J. Contam. Hydrol. 52, 165–186.

Lara, R.H., Briones, R., Monroy, M.G., Mullet, M., Humbert, B., Dossot, M., Naja, G.M., Cruz, R., 2011. Galena weathering under simulated calcareous soil conditions. Sci. Total Environ. 409 (19), 3971–3979.

Lin, Z., 1997. Mineralogical and chemical characterization of wastes from the sulfuric acid industry in Falun, Sweden. Environ. Geol. 30 (3–4), 52–162.

Manceau, A., Marcus, M.A., Tamura, N., 2002. Quantitative speciation of heavy metals in soils and sediments by synchrotron X-ray techniques. Rev. Mineral. Geochem. 49 (1), 341–428.

Mantha, H., Schindler, M., Hochella, M.F., 2019. Occurrence and formation of incidental metallic Cu and CuS nanoparticles in organic-rich contaminated surface soils in Timmins, Ontario. Environ. Sci. Nano 6 (1), 163–179.

Moncur, M.C., Ptacek, C.J., Lindsay, M.B., Blowes, D.W., Jambor, J.L., 2015. Long-term mineralogical and geochemical evolution of sulfide mine tailings under a shallow water cover. Appl. Geochem. 57, 178–193.

Nordstrom, D.K., Alpers, C.N., 1999. Negative pH, efflorescent mineralogy, and consequences for environmental restoration at the Iron Mountain Superfund site, California. Prac. Natl. Acad. Sci. USA 96 (7), 3455–3462.

Nordstrom, D.K., Alpers, C.N., Ptacek, C.J., Blowes, D.W., 2000. Negative pH and extremely acidic mine waters from Iron Mountain, California. Environ. Sci. Technol. 34, 254–258.

Nordstrom, D.K., 2011. Hydrogeochemical processes governing the origin, transport and fate of major and trace elements from mine wastes and mineralized rock to surface waters. Appl. Geochem. 26, 1777–1791.

Ostergren, J.D., Brown, G.E., Parks, G.A., Tingle, T.N., 1999. Quantitative speciation of lead in selected mine tailings from Leadville, CO. Environ. Sci. Technol. 33, 1627–1636.

Parkhurst, D.L., Appelo, C.A.J., 2013. Description of input and examples for PHREEQC version 3: a computer program for speciation, batch-reaction, one-dimensional transport, and inverse geochemical calculations (No. 6-A43). US Geological Survey.

Petrunic, B.M., Al, T.A., 2005. Mineral/water interactions in tailings from a tungsten mine, Mount Pleasant, New Brunswick. Geochim. Cosmochim. Ac. 69, 2469–2483.

Petrunic, B.M., Al, T.A., Weaver, L., 2006. A transmission electron microscopy analysis of secondary minerals formed in tungsten-mine tailings with an emphasis on arsenopyrite oxidation. Appl. Geochem. 21, 1259–1273.

Petrunic, B.M., Al, T.A., Weaver, L., Hall, D., 2009. Identification and characterization of secondary minerals formed in tungsten mine tailings using transmission electron microscopy. Appl. Geochem. 24, 2222–2233.

Ravel, B., Newville, M., 2004. ATHENA, ARTEMIS, HEPHAESTUS: data analysis for X-ray absorption spectroscopy using IFEFFIT. J. Synchrotron Radiat. 12, 537–541.

Renberg, I., Persson, M.W., Emteryd, O., 1994. Pre-industrial atmospheric lead contamination detected in Swedish lake sediments. Nature 368 (6469), 323–326.

Singer, D.M., Herndon, E., Cole, K., Burkey, M., Morisson, S., Cahill, M., Bartucci, M.A., 2020. Micron-scale distribution controls metal (loid) release during simulated weathering of a Pennsylvanian coal shale. Geochim. Cosmochim. Ac. 269, 117–135.